Doubly excited states of the akaline-earth atoms

Chris H. Greene*

Department of Physics, University of Chicago, Chicago, Illinois 60637

(Received 30 June 1980)

Electron correlations in the alkaline-earth atoms and alkali negative ions, especially as manifested by photoabsorption experiments, are studied using a hyperspherical-coordinate approach. A prototype quantitative calculation of the Be photoabsorption spectrum near the 2s and 2p thresholds, allowing for nonadiabatic transitions between potential curves for the first time and hence for autoionization, shows the formation of the " + "-type and " − "-type eigenmodes in the two-electron wave function. This has strong implications for the spectra of Be and other atoms, and permits a unified interpretation of their discrete and continuum oscillator strength.

I. INTRODUCTION

Madden and Codling[1] first observed the doubly excited autoionizing states of helium using synchrotron radiation. Their spectra showed that different $^1P^0$ Rydberg series have reduced decay widths which differ by one to three orders of magnitude. Close-coupling[2] and configuration-mixing[3] calculations of the spectrum reproduced the observations level by level, but did not provide a grouping of levels having similar properties. This grouping emerged later from the studies of Macek[4] and Fano,[5] showing that levels with similar decay widths belong to the same "adiabatic potential curve" $U_\mu(R)$ for the motion of an electron pair along a hyperspherical radius $R = (r_1^2 + r_2^2)^{1/2}$. This method was developed further by Lin,[6] who predicted a similar grouping of excitation channels in H⁻.

In this article, I extend the hyperspherical method to treat two electrons outside a closed-shell ionic core, rather than a bare nucleus only. This extension follows an outline by Fano[7] in simplified form. It aims at interpreting extensive experimental observations of two-electron spectra in the alkaline-earth atoms and in the alkali negative ions, which can be summarized as follows:

(i) Autoionizing $^1P^0$ Rydberg levels (e.g., $2pns$ in Be) are nearly two orders of magnitude broader than the corresponding levels in He.[8,9]

(ii) Quantum defects[10,11] and oscillator strengths[8,12] in the discrete spectra (e.g., $2snp$ $^1P^0$ in Be) depend on n irregularly in contrast with the predictions of independent electron (Hartree-Fock) calculations.

(iii) Multichannel quantum defect theory (MQDT) fits to the energy levels in Ca, Sr, and Ba (Ref. 13) have required the introduction of strongly energy-dependent parameters, in contrast to most previous MQDT applications.[14] Also the angles characterizing channel mixing and the differences between quantum defects are nearly equal for all

of these atoms.[13]

(iv) Photodetachment of the alkali negative ions K⁻, Rb⁻, and Cs⁻ shows resonances just below the first excited $^2P^0$ state of the alkali atom,[15-17] whose autodetaching strength (i.e., the ratio of width to binding energy) is nearly an order of magnitude larger than for Feshbach resonances in H⁻.

(v) Excitation cross sections of the alkali resonance lines by electron collisions are larger than geometric.[18-20] While integrated cross sections are similar to those for hydrogen, the polarization of the alkali fluorescence shows qualitatively different features.[19] A large number of electron-alkali resonances have been observed though most are not yet identified.[21]

Close-coupling and configuration-mixing calculations[12,22-30] have successfully reproduced many of these results individually. Construction of a unified picture of their dynamical origin requires a different approach however, as in the case of helium.

Over the energy range considered here ($\hbar\omega < 15$ eV) the electrons in the closed-shell ionic core cannot be excited, but only screen the outermost two electrons from the nucleus. Since the response of a single electron to this screened radial potential depends strongly on its orbital angular momentum l, the energy levels E_{nl} with different l are nondegenerate for the singly charged alkaline-earth ions in contrast to He⁺. This removal of degeneracies opens the possibility of an autoionizing transition occurring within a shell, as in the strong $2pns \rightarrow 2s\epsilon p$ process in Be. Such a process requires little excitation of the Be⁺ core and so the transition matrix element, $(2s\epsilon p |r_{12}^{-1}| 2pns)$ in perturbation theory, is likely to be large. The point of view of this article differs from this independent electron picture. I evaluate instead the eigenmodes of the full short-range Be Hamiltonian (including r_{12}^{-1}) and show them to be approximately of the form $2s\epsilon p \pm 2pns$ suggested by Cooper, Fano, and Prats[31] for He and later documented by Macek[4]

and Lin.[6(a),6(c)] The channel mixing is expected to be similarly strong for other two-electron systems as well.

From the hyperspherical viewpoint, autoionization results from a nonadiabatic transition between two adiabatic potential curves. By explicitly including nonadiabatic couplings between the potential curves $U_\mu(R)$ and obtaining autoionization decay widths, my work goes substantially beyond the previous hyperspherical calculations which were confined to the adiabatic (i.e., Born-Oppenheimer) approximation. The eventual inclusion of the interchannel couplings

$$P_{\mu\nu}(R) = (\phi_\mu | \partial \phi_\nu/\partial R)$$

was envisioned by Macek, though its technology had never yet been explored. The calculations reported here are intended to survey for the first time time a broad class of nonadiabatic effects. State-of-the-art accuracy has not been attempted here, but it should be possible, nevertheless, to systematize the hyperspherical method and enhance its predictive power.

This article will consider only low-energy double excitations, well below the threshold for escape of both outer electrons. It remains for future studies to connect quasiadiabatic studies like this one, involving just a few hyperspherical potential curves, to the Wannier-Rau-Peterkop[32-34] treatments of two-electron escape, which involve an infinite number of potential curves. Preliminary elements of this connection have recently been formulated,[35] though their full implementation has not yet been explored.

This paper will be organized in the following manner. Section II reviews the hyperspherical formulation of Macek, Fano, and Lin, including the screening effects of a closed-shell, many-electron core. Section II then discusses adiabatic potential curves for Be and K⁻ and describes the pattern of radial correlations in the channel wave functions. Section III presents the calculation of Be photoionization and gives a unified picture of the oscillator strength distribution in the discrete and continuous spectra. Section IV discusses the relevance of the Be results to the remaining observations (i)–(v) above, and a summary is given in Sec. V.

II. THE HYPERSPHERICAL FORMULATION

The stationary-state Schrödinger equation for two electrons in the screened potential of a nucleus takes the form (in a.u.)

$$\left(-\tfrac{1}{2}\nabla_1^2 - \tfrac{1}{2}\nabla_2^2 - \frac{Z(r_1)}{r_1} - \frac{Z(r_2)}{r_2} + \frac{1}{r_{12}}\right)\Psi = E\Psi. \tag{1}$$

In Eq. (1), r_1 and r_2 are the electron distances from the nucleus, r_{12} is the electron separation, and $Z(r)$ represents the nuclear charge as screened by N_C closed-shell core electrons. At small distances $r \sim 0$, $Z(r)$ approaches the nuclear charge Z_0, while $Z(r) \to Z_0 - N_C$ at large radii. Between these two extremes $Z(r)$ will be taken as a standard Hartree-Slater function.[36] In the hyperspherical coordinates,

$$R = (r_1^2 + r_2^2)^{1/2}, \quad \alpha = \arctan(r_2/r_1). \tag{2}$$

Equation (1) becomes[37]

$$\left(\frac{\partial^2}{\partial R^2} + \frac{1}{4R^2} + (E - \hat{U})\right)\psi = 0, \tag{3}$$

$$\hat{U}(R;\Omega) = \frac{1}{R^2}\left(-\frac{1}{2}\frac{\partial^2}{\partial\alpha^2} + \frac{\hat{l}_1^2}{2\cos^2\alpha} + \frac{\hat{l}_2^2}{2\sin^2\alpha}\right)$$
$$- \frac{Z(R\cos\alpha)}{R\cos\alpha} - \frac{Z(R\sin\alpha)}{R\sin\alpha} + \frac{1}{r_{12}}, \tag{4}$$

where $\hat{l}_1^2$ and $\hat{l}_2^2$ are the orbital angular momenta of the electrons and Ω denotes all angular variables. Note that all first derivatives in R and in α have been eliminated in Eqs. (3) and (4).

To solve Eq. (3), Ref. 4 assumed a slow dependence on R and constructed adiabatic potential curves $U_\mu(R)$ and eigenfunctions $\phi_\mu(R;\Omega)$ which satisfy

$$\hat{U}(R;\Omega)\phi_\mu(R;\Omega) = U_\mu(R)\phi_\mu(R;\Omega). \tag{5}$$

Expansion of ψ into the ϕ_μ,

$$\psi = \sum_\mu \phi_\mu(R;\Omega)F_\mu(R), \tag{6}$$

transforms the six-variable Schrödinger equation to an infinite set of coupled differential equations in R for $F_\mu(R)$[38]:

$$\left\{\left[\mathbf{1}\frac{d}{dR} + \underline{P}(R)\right]^2 + \frac{1}{4R^2} + 2[E - \underline{U}(R)]\right\}\vec{F}(R) = 0, \tag{7}$$

where

$$P_{\mu\nu}(R) = \int d\Omega\, \phi_\mu(R;\Omega)\frac{\partial}{\partial R}\phi_\mu(R;\Omega), \tag{8}$$

$$U_{\mu\nu}(R) = U_\mu(R)\delta_{\mu\nu}. \tag{9}$$

By ignoring off-diagonal terms of $\underline{P}$ in Eq. (7), Macek[4] calculated adiabatic energy levels of doubly excited helium obtaining good agreement with experiment and with other calculations. Moreover, autoionizing levels belonging to the same potential curve were associated with previously calculated states having comparable reduced decay widths, while the widths of levels belonging to different curves varied by one to three orders of magnitude. Note that this quasiseparability of the motion in R has no simple physical interpretation analogous to

the Born-Oppenheimer approximation for the vibrations of molecules. Rather the quasiseparability is interpreted as evidence for a new approximate constant of the motion for the two-electron system.

At small R the kinetic-energy terms in $\hat{U}(R;\Omega)$ dominate and are separable. $U_\mu(R)$ represents then a repulsive barrier arising from the centrifugal kinetic energy in both the true angular variables $(\Theta_1, \varphi_1), (\Theta_2, \varphi_2)$ and the mock angle α,

$$U_\mu(R) \underset{R\to 0}{\to} (l_{1\mu} + l_{2\mu} + 2m_\mu + 2)^2/2R^2 + O(R^{-1}). \quad (10)$$

Each potential curve U_μ is thus labeled here by orbital angular momenta $l_{1\mu}, l_{2\mu}$ of the two electrons, and by a third integer quantum number $m_\mu \geq 0$, the number of nodes of the wave function in α. The good quantum numbers near $R = 0$ are then $l_{1\mu}, l_{2\mu}, m_\mu, L, M_L, S$, and M_S.

The opposite limit $R \to \infty$ corresponds to either $r_1 \to \infty$ or $r_2 \to \infty$ in the energy range considered here, below the double-escape threshold. Accordingly at $R \to \infty$ one electron remains in the potential well near $\alpha \sim 0$ or $\alpha \sim \pi/2$, forming a bound state of the alkali-like ion at energy E_{nl}. The other electron retains then the energy $E - E_{nl}$ for its motion in R. Hence the potential curve assumes the large-R form

$$U_\mu(R) \underset{R\to\infty}{\to} E_{n_\mu l_\mu} - (Z_0 - N_C - 1)/R + O(R^{-2}). \quad (11)$$

(For neutral alkaline-earth atoms $Z_0 - N_C - 1 = 1$.) In this limit Eq. (5) reduces to the usual single-electron radial equation

$$\left(-\frac{1}{2}\frac{d^2}{dr^2} + \frac{l_\mu(l_\mu + 1)}{2r^2} - \frac{Z(r)}{r}\right)P_{n_\mu l_\mu}(r) = E_{n_\mu l_\mu}P_{n_\mu l_\mu}(r),$$

$$(12)$$

where r is the smaller of (r_1, r_2). Also in this limit, Eq. (7) for the motion in R reduces to the usual close-coupling equations[22] for one electron far from an atom or ion.

At intermediate R, Eq. (5) must be solved numerically. References 4 and 6 performed this numerical solution by expanding ϕ_μ into ordinary spherical harmonics coupled to form a given total orbital angular momentum $\vec{L} = \vec{l}_1 + \vec{l}_2$:

$$\phi_\mu(R;\Omega) = \sum_{l_1 l_2} g_\mu^{l_1 l_2}(R;\alpha) Y_{l_1 l_2 L M_L}(\Theta_1\varphi_1;\Theta_2\varphi_2).$$

$$(13)$$

This reduces Eq. (5) to coupled ordinary differential equations in α for $g_\mu^{l_1 l_2}(R;\alpha)$ and $U_\mu(R)$. Because the range of α is finite and $g_\mu^{l_1 l_2}$ vanishes at $\alpha = 0$ and $\alpha = \pi/2$, the eigenvalues $U_\mu(R)$ at each R form a discrete set with no continuum. The requirement of antisymmetry of ψ is formulated simply as a boundary condition:

$$g_\mu^{l_1 l_2}(R;\pi/4) = (-1)^{l_1 + l_2 - L + S} g_\mu^{l_2 l_1}(R;\pi/4)$$

$$\frac{\partial}{\partial\alpha}g_\mu^{l_1 l_2}(R;\pi/4) = (-1)^{l_1 + l_2 - L + 1}\frac{\partial g_\mu^{l_2 l_1}}{\partial\alpha}(R;\pi/4). \quad (14)$$

Further details of the α integration closely follow the discussion in Ref. 4. The expansion (13) in $(l_1 l_2)$ converges in only a few terms, since the coupling of different $(l_1 l_2)$ components [by $1/r_{12}$ in Eq. (4)] is strong only in limited ranges of R.[6(a)]

A. $^1P^0$ potential curves

With this approach the $^1P^0$ adiabatic potential curves for Be and K^- have been calculated. Figure 1 compares them to earlier results for He and H^-. Each of these four figures shows a common feature: at small R, $U_\mu(R)$ forms a repulsive barrier as in Eq. (10), while at large R, $U_\mu(R)$ flattens out and converges to a one-electron energy level E_{nl} as in Eq. (11). For He and Be each potential curve contains an infinite number of bound (or autoionizing) levels because of the attractive Coulomb potential at large R. The absence of the Coulomb tail for H^- and K^- changes things. For K^- each potential curve contains either no levels or one quasibound level, since the long-range polarizability potential supports only a finite number of bound states. This is also true for the "$sp+$" and "pd" curves of H^-, but the "$sp-$" curve does contain an infinite number of very closely spaced autodetaching levels, since it represents a sufficiently attractive R^{-2} potential at large R.[39,40] Beyond these similarities of all the potential curves, there is a qualitative difference in Be and K^-, which is the absence of the diabatic crossings at $R \sim 7.5$ a.u. in He and $R \sim 13.5$ a.u. in H^-. This is because the $2s$ and $2p$ levels of Be^+ (or $4s$ and $4p$ of K) are non-degenerate which forces the potential curves apart near the crossing. The avoided crossing near $R \sim 4-5$ a.u. in Be will be seen in Sec. III to have important effects intermediate between those expected from adiabatic and diabatic approximations, and to be responsible for the very large widths of the $2pns$ autoionizing states.

The potential energy in Eq. (4) consists of two attractive terms near $\alpha \sim 0$ and $\alpha \sim \pi/2$ representing the screened nuclear attraction, and a repulsive term $1/r_{12}$ which is maximum at $\alpha = \pi/4$. The lowest value of this repulsion at $\alpha = \pi/4$ (as a function of $\cos\theta_{12}$) occurs when the electrons are in opposite directions $\hat{r}_2 = \hat{r}_1$, i.e., at $\theta_{12} = \pi$. This saddle point of the potential energy has the value[37] $U_s(R) = \sqrt{2}(4Z_0 - 1 - 4N_C)/R$, in Rydbergs, relative to the threshold for two-electron escape; here, $Z_0 - N_C = 2$ for He and Be and $Z_0 - N_C = 1$ for H^- and K^-. Thus, when $U_\mu(R) > U_s(R)$ the local kinetic energy at $\alpha = \pi/4$ will be positive and ψ is oscillatory,
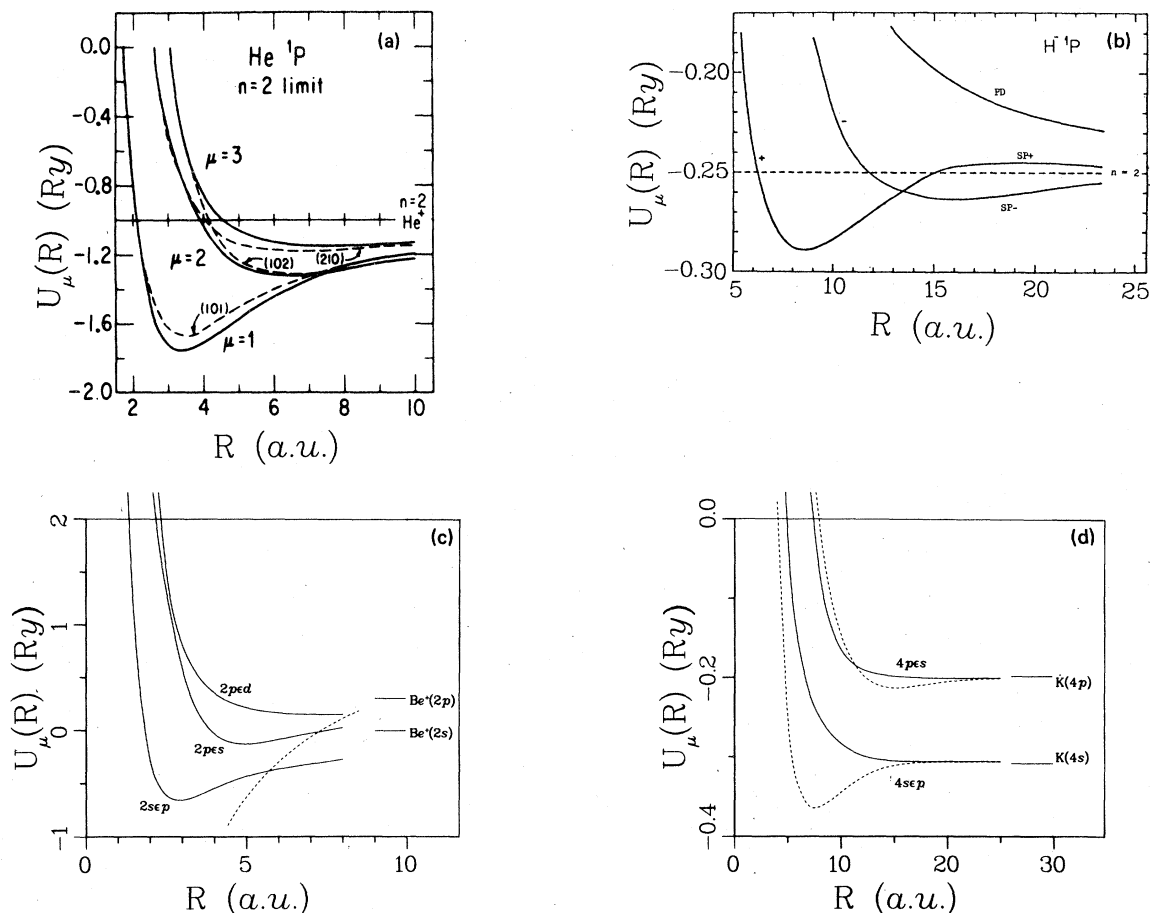
FIG. 1. Comparison of the lowest two-electron $^1P^0$ hyperspherical potential curves without and with a many-electron core: (a) He from Ref. 6(a); dashed curves are potentials obtained by ignoring sp-pd couplings; (b) H⁻ from Ref. 6(c); (c) Be, present calculation; dashed curve shows the level of the potential ridge associated with avoided crossings. The zero of the energy scale has been set at the $2s$ threshold; (d) K⁻, present calculation (ignoring pd and higher partial waves); dashed curve shows the $^3P^0$ potential curves.

at least in the most attractive orientation $\theta_{12} = \pi$. When $U_\mu(R) < U_s(R)$, however, the wave function ψ will be exponentially damped at all orientations θ_{12}. Accordingly, the radius $R_{c\mu}$ at which $U_\mu(R_{c\mu})$ ~ $U_s(R_{c\mu})$ marks the transition from small-R to large-R behavior, i.e., the locus of avoided crossings. (In fact, the crossings occur always at a somewhat smaller radius $R \lesssim R_{c\mu}$).

B. $^1P^0$ radial correlations

The transition from $R < R_{c\mu}$ to $R > R_{c\mu}$ is apparent in the α-dependent channel wave functions $g_\mu^{l_1 l_2}(R;\Omega)$ of Be plotted in Fig. 2 for $(l_1 l_2) = (10)$. The wave function associated with the lowest potential curve $2s\epsilon p$ is shown in Fig. 2(a), and has R_{c1} ~ 5. At $R < R_{c1}$ $g_1^{10}(R;\alpha)$ oscillates freely in α with a wavelength which is longest near $\alpha = \pi/4$, where a broad antinode is centered. The wave

function in this range of R shows a high probability for the two electrons to have nearly equal radii, i.e., to achieve double excitation. As R increases through the transition region $R \gtrsim R_{c1}$, this behavior changes rapidly, with $g_1^{10}(R;\alpha)$ becoming exponentially damped in the region α ~ $\pi/4$. Moreover, the probability is now pushed entirely into one valley, in this case the α~0 valley, reflecting how one electron remains attached to the ion at large R where $g_1^{10}(R;\alpha)$ becomes proportional to the Be⁺$(2s)$ radial wave function P_{2s}-$(R\alpha)$. Analogous behavior occurs along the $2p\epsilon s$ potential curve, with R_{c2} ~ 6.5. But in this case the $R < R_{c2}$ region has a *node* in the vicinity of $\alpha = \pi/4$, implying a *much lower probability for double excitations* than for the $2s\epsilon p$ curve. As R increases to $R \gtrsim R_{c2}$, $g_2^{10}(R;\alpha)$ is pushed into the potential valley at α ~ $\pi/2$, where it becomes proportional to $P_{2p}[R(\pi/2 - \alpha)]$.
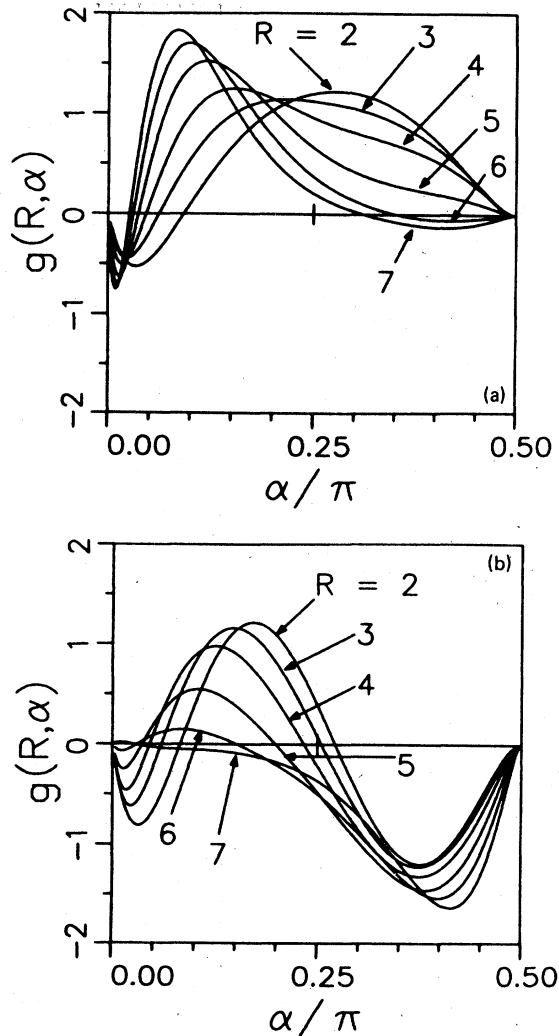
FIG. 2. Adiabatic "sp" channel wave functions associated with the lowest two Be potential curves: (a) $2s\epsilon p$, $\mu=1$; (b) $2p\epsilon s$, $\mu=2$.

This behavior of the $g_{\mu}^{l_1 l_2}(R;\alpha)$ for Be and K$^-$ bears important similarities to He and H$^-$, as well as a crucial difference. The helium wave functions, [(Fig. 5 of Ref. 6(a)] also oscillate freely for $R < R_{c\mu}$, forming "+"-type waves with an antinode near $\alpha = \pi/4$, and more repulsive "−"-type wave with a node near $\alpha = \pi/4$. Furthermore, as R increases through $R_{c\mu}$, the helium wave functions are also deflected away from the ridge $\alpha = \pi/4$ into the potential valleys. But this deflection occurs much more smoothly for helium than beryllium. The degeneracy of the $2s$ and $2p$ levels of He$^+$ leads to a quasidegeneracy of potential curves $U_{\mu}(R)$ in the two valleys. This degeneracy is split according to symmetry or antisymmetry about $\alpha = \pi/4$ even when the two valleys are separated by

a potential barrier at large R. In contrast the Be potential curves converge as $R \to \infty$ to different levels of Be$^+$, $2s$ and $2p$. No resonance of the $g_{\mu}^{10}(R;\alpha)$ between the two valleys is then possible, and each wave function remains confined mainly to one valley or the other, as shown in Fig. 2. Nevertheless, Sec. III will demonstrate how the "+" and "−" character established at short range is preserved at larger R (for sufficiently high energy) by the full wave function breaking up into a superposition of the adiabatic wave functions with nearly equal amplitudes.

C. Electron correlations for other values of L and S

The preceding argument does not apply to states having $L = 0$, and hence $l_1 = l_2$; Eq. (14) implies that $^1S^e$ states are automatically symmetric under $\alpha \to \pi/2 - \alpha$, while $^3S^e$ states are antisymmetric. Thus the wave function $g_{\mu}^{l_1 l_1}(R;\alpha)$ can resonate between $\alpha \sim 0$ and $\alpha \sim \pi/2$ at all R irrespective of the screening potential, and S states of Be and He autoionize at a comparable rate. However, the antisymmetry of the ^3S $g_{\mu}^{l_1 l_1}(R;\alpha)$ about $\alpha = \pi/4$ implies that triplet "−"-type states should decay much more slowly than the symmetric "+"-type ^1S states, as is verified by experiment.

In fact, singlet states are expected to autoionize faster than triplets even from the conventional independent electron picture, since triplet wave functions have a node at the location $\vec{r}_1 = \vec{r}_2$ while singlets have an antinode. Consequently the transition-matrix element $\langle \psi_1 | 1/r_{12} | \psi_2 \rangle$ is much larger for singlet states. This statement can be amplified by adopting the hyperspherical viewpoint. For helium the $^3P^0$ potential curves analogous to Fig. 1(a) for $^1P^0$ show no diabatic crossing between the "+" and "−" channels, but rather behave adiabatically. When the degeneracy of $2s$ and $2p$ is broken, as in Be, the $^3P^0$ potential curves are repelled even further, implying a less drastic breakdown of the adiabatic approximation than for $^1P^0$ symmetry. The largest breakdowns of adiabatic behavior, and accordingly the strongest channel mixings, are thus expected for singlet states with $l_1 \neq l_2$. A good example is the interaction between $4s\epsilon d$ and $3dns$ $^1D^e$ channels of calcium, which is known experimentally[13] to be comparable in strength to the $^1P^0$ channel interaction.

The study of the $^1S^e$ ground states of all these two-electron atoms can thus be conducted here within the adiabatic approximation, i.e., ignoring channel coupling. The $^1S^e$ potential curves of Be are K$^-$ are shown in Fig. 3. The energy levels obtained by solving Eq. (7), ignoring $P_{\mu\nu}(R)$, are given in Table I. The agreement with experiment is reasonably good, showing that this model contains the correct qualitative physical elements.
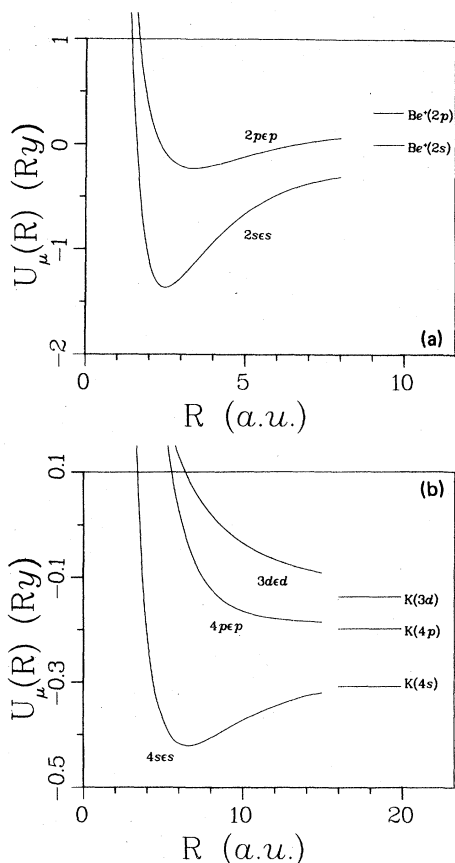
FIG. 3. Ground-state $^1S^e$ hyperspherical potential curves: (a) Be; (b) K⁻. [The energy scale for Be has been shifted as in Fig. 1(c).]

III. FULL TREATMENT OF THE Be SPECTRUM

Excitation and charge transfer in low-energy atom-atom or ion-atom collisions generally result from nonadiabatic transitions localized at avoided crossings between two potential curves of the composite molecular system. The present section demonstrates quantitatively that autoionization and atomic excitation by low-energy electrons can be similarly described as a localized nonadiabatic transition between two hyperspherical potential curves. Here it will be shown for the first time that a specific low-energy process involves only two terms in the hyperspherical expansion Eq. (6). Inclusion of only $2s\epsilon p$ and $2p\epsilon s$ of Fig. 1(c) is

TABLE I. $^1S^e$ binding energies.

System	Adiabatic (Ry)	Experiment (Ry)
Be $2s^2$	0.740	0.685
K⁻ $4s^2$	0.032	0.037

sufficient to describe autoionizing $^1P^0$ $2pns$ resonances of Be, which was by no means a foregone conclusion. Note also that the additional crossing of the Be potential curves $2p\epsilon d$ and $2p\epsilon s$ near $R = 3$ in Fig. 1(c) is quite diabatic, implying that $2p\epsilon d$ interacts only weakly with the other channels. Accordingly, the remainder of Sec. III will consider only the $2s\epsilon p$ (curve label $\mu = 1$) and $2p\epsilon s$ ($\mu = 2$) potential curves of $^1P^0$ Be.

A. Adiabatic calculation of $^1P^0$ energy levels

The present prototype study of $^1P^0$ Be has been chosen specifically *because* nonadiabatic effects are strong and thus nonperturbative. The most obvious manifestation of this nonadiabatic channel mixing is the large autoionizing decay width[8] of the $2pns$ levels which belong to the $2p\epsilon s$ potential curve of Fig. 1(c) and decay into the $2s\epsilon p$ continuum. Before treating the autoionization spectrum (Sec. III E), however, I will first examine the weaker nonadiabatic effects already present in the energy levels of the discrete $2snp$ states.

Nonadiabatic effects depend on the magnitude of the velocity coupling matrix $P_{12}(R)$ of Eq. (8), shown in Fig. 4. This coupling peaks in the middle of the avoided crossing at $R \sim 5$, where the wave function $g_\mu^{10}(R;\alpha)$ breaks away from the ridge ($\alpha = \pi/4$) into the potential valleys ($\alpha \sim 0$ or $\pi/2$) over a small interval in R. The strong interaction region is reasonably well localized with a width of about 2 a.u., although it is broader than the usual avoided crossings between molecular potential curves. While $P_{12}(R)$ rises again from $R \sim 2$ toward $R \sim 0$, this small-R region contributes little to the nonadiabatic transition probability. This is because the effectiveness of the coupling is measured by the size of the dimensionless ratio
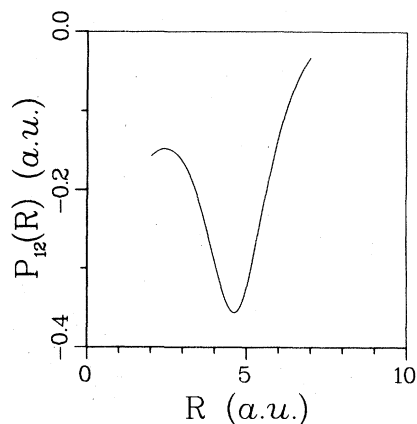

FIG. 4. Nonadiabatic coupling-matrix element P_{12} $= \langle \phi_1 \mid \partial\phi_2/\partial R \rangle$ between lowest two $^1P^0$ potential curves of Be.

$P_{12}^2(R)/[U_1(R) - U_2(R)]$,

rather than by P_{12} itself. At small R, $U_\mu(R)$ rises
as R^{-2}, which thus renders the coupling ineffective.

The adiabatic approximation, strictly speaking,
entirely disregards $P_{\mu\nu}(R)$ in the radial Eq. (7).
This method was used to calculate $^1S^e$ levels in
Sec. II. A variant of this approach introduced by
Macek[4] has in fact been used more often, and adds
to $U_\mu(R)$ the "diagonal coupling term"

$$-W_{\mu\mu}(R) = -\tfrac{1}{2}(\underline{P}^2)_{\mu\mu} = -\frac{1}{2}\left(\phi_\mu \left| \frac{\partial^2 \phi_\mu}{\partial R^2}\right.\right) . \quad (15)$$

The antisymmetry of $\underline{P}_{\mu\nu}$ implies that $-W_{\mu\mu}$ gives
a repulsive contribution to the potential energy.
Inclusion of $W_{\mu\mu}$ ensures that the potential energy
at large R reduces to the independent-electron
form[4] expected for the e-Be$^+$ potential, through
order R^{-2}:

$$U_\mu(R) - W_{\mu\mu}(R) \xrightarrow[R\to\infty]{} E_{n_\mu l_{1\mu}} - 1/R$$

$$+ l_{2\mu}(l_{2\mu}+1)/2R^2 + O(R^{-3}) . \quad (16)$$

Furthermore, the lowest adiabatic energy level
calculated in the lowest potential curve of each
(L,S,π) is a lower bound to the exact level if $W_{\mu\mu}$
is omitted, while it is an upper bound if $W_{\mu\mu}$ is
included.[41]

Thus the difference between energy levels cal-
culated by these two methods reflects the impor-
tance of nonadiabatic effects. Table II shows the
quantum defects of the lowest Be $2snp$ $^1P^0$ bound
levels obtained with these two approximations.
The experimental $2s2p$ quantum defect lies rough-
ly midway between the two calculations, which
differ by a large amount: 0.30 out of a maximum
discrepancy of 0.50 (modulo 1). A similar calcu-
lation by Miller and Starace[42] of $^1P^0$ He quantum
defects shows a difference of only 0.09 between
the alternative methods, thus verifying that non-
adiabatic (or nondiabatic) effects are far less im-
portant for He than for Be.

Another relevant feature of Table II is the unex-
pected jump of the experimental quantum defect
from $\mu(2s2p)=0.166$ to $\mu(2s3p)=0.29$, which is an
illustration of item (ii) of Sec. I. This jump is not
reproduced even qualitatively by either adiabatic
approximation and is a clear illustration of a non-

TABLE II. $2snp$ $^1P^0$ discrete levels of Be.

n	$\mu^{\text{expt.}}$	μ (adiabatic)	μ (adiabatic with $W_{\mu\mu}$)
2	0.166	0.290	−0.021
3	0.295	0.259	0.007
4	0.289	0.256	0.005

adiabatic coupling effect, to be interpreted further
in Sec. III D below.

B. Solution of the coupled equations in R

To understand the Be autoionization dynamics
and the erratic level structure of the discrete
spectrum, I will now incorporate the nonadiabatic
off-diagonal terms of Eq. (7). The channel inter-
action will be treated directly by truncating Eq. (7)
to two channels only, and then utilizing Klar's re-
duction of the two coupled equations to a set of four
first-order ordinary differential equations[38(a)]:

$$\frac{dF_1}{dR} + P_{12}F_2 + G_1 = 0 ,$$

$$\frac{dF_2}{dR} - P_{12}F_1 + G_2 = 0 ,$$

$$\frac{dG_1}{dR} + P_{12}G_2 - 2(E - \tilde{U}_1)F_1 = 0 ,$$

$$\frac{dG_2}{dR} - P_{12}G_1 - 2(E - \tilde{U}_2)F_2 = 0 . \quad (17)$$

Here, $F_1(R)$ and $F_2(R)$ are the radial eigenfunc-
tions of Eq. (6) and the equation defines $G_i(R)$ as

$$-(dF_i/dR + \textstyle\sum_j P_{ij}F_j) .$$

The potential curves $2\tilde{U}_i(R)$ include the term
$1/4R^2$ of Eq. (7), in addition to the $U_i(R)$ shown in
Fig. 1(c).

One point which requires some discussion is the
validity of truncating Eq. (7) to two channels only.
In fact, this truncation is not unique, as seen from
a different form of Eq. (7) given in Ref. 4:

$$\left(\frac{d^2}{dR^2} + \frac{1}{4R^2} + 2(E - U_\mu)\right)F_\mu + 2\sum_\nu \left(P_{\mu\nu}\frac{d}{dR} + W_{\mu\nu}\right)F_\nu = 0 , \quad (18)$$

with

$$W_{\mu\nu}(R) = \frac{1}{2}\left(\phi_\mu \left| \frac{\partial^2 \phi_\nu}{\partial R^2}\right.\right). \quad (19)$$

Equations (18) and (7) are identical if no truncation
of channels is made, in which case

$$W_{\mu\nu}(R) = \frac{1}{2}\sum_\gamma P_{\mu\gamma}P_{\gamma\nu} + \frac{1}{2}\frac{dP_{\mu\nu}}{dR} . \quad (20)$$

This relation is no longer satisfied if the summa-
tion over γ is truncated to $\gamma \leqslant 2$, as implied by Eq.
(17). The equality (20) is satisfied near the
avoided crossing at $R \sim 5$, but at larger R, $P_{12}(R)$
decays as R^{-3}, while $W_{11}(R)$ and $W_{22}(R)$ remain of
order R^{-2}. To ensure that the diagonal terms in
the large-R form of Eq. (17) reduce to the inde-
pendent-electron form Eq. (16), the potential
$\tilde{U}_\mu(R)$ has been modified to the form

$$\bar{U}_\mu(R) = U_\mu(R) - \tfrac{1}{8}R^2 - W_{\mu\mu}(R) - \tfrac{1}{2}P_{12}^2(R), \quad (21)$$

with $W_{\mu\mu}(R)$ calculated directly from $(\phi_\mu\,|\partial^2\phi_\mu/\partial R^2)$. The subtraction of $\tfrac{1}{2}P_{12}^2(R)$ ensures that the nonadiabatic effects are not counted twice.

This modified potential attains the Coulombic and centrifugal form of Eq. (16) to good accuracy beyond $R_0 = 14$ a.u., so the off-diagonal coupling $P_{12}(R)$ was neglected beyond that radius. Consequently the solutions of Eq. (17) can be expressed as linear combinations of well known Coulomb functions for all $R \geq R_0$, in the approximation that effects of longer-range potentials (e.g., polarization) are negligible at large R. This simplifies the calculation considerably, limiting the need for an explicit numerical integration of the coupled Eq. (17) to a "reaction zone" $R \leq R_0$. This approach is thus similar to R-matrix calculations,[43,44] which also solve the Schrödinger equation only within a limited volume of space; in the present application the value of R_0 is just large enough to contain the entire valence shell.

Once the potential curves $U_\mu(R)$ and the couplings $W_{\mu\mu}(R)$ and $P_{\mu\nu}(R)$ were calculated and stored, the radial integration of Eq. (17) at different energies was straightforward and required little computer time and storage. On an IBM 3033, less than thirty seconds of CPU time were needed to solve the radial equations at twenty energies. (This time includes also the matching to Coulomb functions at $R = R_0$, determination of the reaction matrix, and calculation of dipole matrix elements.) In contrast, the energy independent part of the calculation described in Sec. II, which consists of determining the potential curves and couplings, required longer time, in the neighborhood of five minutes. This method of calculation differs in a fundamental way from a more common close-coupling method. Most importantly, an examina-

tion of intermediate pieces of the hyperspherical calculation, such as the potential curves, provides a qualitative interpretation of many dynamical features. In addition, the close-coupling method has exchange terms which make the coupled equations *integrodifferential* (though they can be transformed to purely differential form by adding subsidiary equations[45]). Accordingly, the close-coupling calculations are numerically more efficient if only a few energies are studied, whereas the hyperspherical approach should be more appropriate if the equations are to be solved at many energies.

C. Energy dependence of the short-range MQDT scattering parameters

The four coupled Eqs. (17) have in principle four independent solutions, but I will consider only two of these which are regular at $R = 0$. Particular superpositions of these two solutions are singled out by physical boundary conditions at large R.

Since the potential is Coulombic at large R these solutions can be represented as a linear combination of regular and irregular Coulomb wave functions (f_i, g_i) in each channel i, normalized per unit energy and at energy $\epsilon_i = E - E_{n_i l_i}$. These coefficients, which then represent the mixing of channels discussed in Sec. IIB, are automatically free of the main nonanalyticities at threshold due to the long-range Coulomb field; residual nonanalyticities could be removed by further renormalization of the pair (f_i, g_i) (Ref. 46, Sec. IIC). One standard representation of multichannel wave functions in scattering theory utilizes a base set of independent solutions, each of which includes the regular Coulomb function f_i in a single channel only. The admixture K_{ij} of irregular functions g_j then represents the effects of channel mixing generated at smaller distances,

$$\begin{aligned}
\chi_1' &= \phi_1(R;\Omega)[f_1(R) - g_1(R)K_{11}] - \phi_2(R;\Omega)g_2(R)K_{21} \\
\chi_2' &= -\phi_1(R;\Omega)g_1(R)K_{12} + \phi_2(R;\Omega)[f_2(R) - g_2(R)K_{22}]
\end{aligned} \right\} \; R \geq R_0, \quad (22)$$

Here I utilize instead an alternative base set of solutions for which the reaction matrix K_{ij} is diagonal, and which is represented by phase shifts $\pi\mu_\alpha$ equal for all channels. These eigensolutions have the form

$$\psi_\alpha = \phi_1(f_1 \cos\pi\mu_\alpha - g_1 \sin\pi\mu_\alpha)U_{1\alpha}$$
$$+ \phi_2(f_2 \cos\pi\mu_\alpha - g_i \sin\pi\mu_\alpha)U_{2\alpha}, \quad R \geq R_0,$$
$$(23)$$

where

$$K_{ij} = \sum_\alpha U_{i\alpha}\tan\pi\mu_\alpha U_{j\alpha}. \quad (24)$$

The 2×2 real orthogonal matrix $U_{i\alpha}$ is represented in terms of a single channel-mixing angle θ:

$$U = \begin{bmatrix} \cos\theta & \sin\theta \\ -\sin\theta & \cos\theta \end{bmatrix}. \quad (25)$$

This same transformation expresses the $^1P^0$ $e\text{-}Be^+$ scattering matrix in terms of the eigenphase shifts $\pi\mu_\alpha$,

$$S_{ij} = e^{i\sigma_i}\left(\sum_\alpha U_{i\alpha}e^{2i\pi\mu_\alpha}U_{j\alpha}\right)e^{i\sigma_j}, \quad (26)$$

where σ_i is the continuum Coulomb phase shift in channel i. With this notation the probability of a transition from the lower potential curve ($2s\epsilon p$) to the upper curve ($2p\epsilon s$) in a single $e\text{-}Be^+$ collision takes the simple form

$$|S_{12}|^2 = \sin^2 2\theta \, \sin^2 \pi (\mu_1 - \mu_2). \tag{27}$$

This expression shows how a large excitation probability implies that the channel mixing is strong ($\theta \sim \pi/4$) and that the two eigenchannel solutions ψ_α oscillate nearly $90°$ out of phase at $R \gtrsim R_0$ ($|\mu_1 - \mu_2| \sim \frac{1}{2}$).

The results of the numerical solution of coupled equations described in Sec. II B are thus represented in Fig. 5 as plots of the eigen-quantum defects μ_1 and μ_2 and the mixing angle θ against the energy. The energy range extends from the $2snp$ discrete spectrum below the $2s$ level of Be^+, through the autoionizing spectrum between the $2s$ and $2p$ levels, to the open continuum above $Be^+(2p)$ (but still far below the $3snp$ autoionizing states of Be). Note that the plot extends smoothly into the discrete spectrum of Be, in accordance with Refs. 46 and 47. Figure 5 contains all the information necessary to determine the $2snp\ {}^1P^0$ bound-state energies of Be and also the elastic and inelastic $e\text{-}Be^+$ scattering cross sections. Three features of Fig. 5 are especially significant:

(a) Far below the $2s$ and $2p$ thresholds, the two channels are independent and closed. The rapid decrease of μ_1 and μ_2 with ϵ_1 reflects the behavior of single-channel quantum defects in energy ranges where the channel is strongly closed and the functions (f, g) diverge exponentially as discussed in Ref. 48. This energy dependence has the form

$$\mu_i \to n - \nu_i, \quad \epsilon_i \ll - R_0^{-1} \tag{28}$$

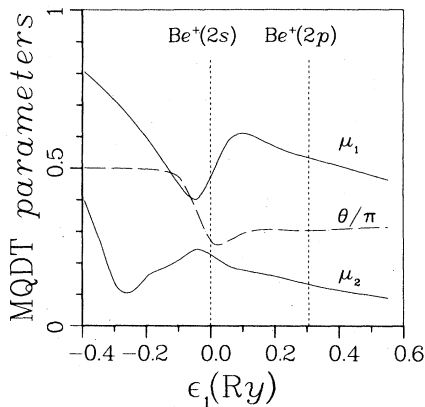FIG. 5. Calculated short-range Be scattering parameters μ_1, μ_2, and θ, as functions of the energy ϵ_1 relative to the $2s$ threshold.

where $\nu_i = (-2\epsilon_i)^{-1/2}$, and $R_0 = 14$ a.u. here. Figure 5 shows this behavior with $\mu_1 \to 1 - \nu_2$ and $\mu_2 \to 2 - \nu_1$. (That μ_1 gets associated with channel 2 and μ_2 with channel 1 is a result of a convention setting θ by $\theta \sim \frac{1}{2}\pi$ at low energies instead of 0.)

(b) The decrease of μ_2 ends around $\epsilon_1 \sim -0.28$, where μ_2 begins to rise. This increase reflects the influence of channel coupling which makes the lower channel more attractive, in accordance with the postadiabatic analysis of Klar and Fano.[38] This rise is responsible for raising the $2s3p$ experimental quantum defect in Table II. Note that this effect of the channel coupling matrix $P_{\mu\nu}$ becomes strong even below the energy at which the channel mixing parameter θ begins to deviate from its low energy limit in accordance with Ref. 38.

(c) As the energy reaches the minimum of the upper ($2p\epsilon s$) potential curve [Fig. 1(c)] at $\epsilon_1 \sim -0.15$, the mixing angle makes a rapid transition from its no-mixing value $\theta \sim \frac{1}{2}\pi$ to almost equal mixing $\theta \sim \frac{1}{4}\pi$ at $\epsilon_1 \sim 0$. In the terminology of Sec. II this transition describes the breaking of the wave functions ψ_α away from the potential ridge as R increases through the range $R \gtrsim R_{c\mu}$. These wave functions defined by Eq. (23) for $R \geqslant R_0$ extrapolate into the range of lower $R < R_{c\mu}$ where they coincide with ϕ_2 and ϕ_1, respectively. At an energy lower than the minimum of the $2p\epsilon s$ channel ψ_2 is necessarily deflected adiabatically into the more attractive $2s$ valley ($\alpha \sim 0$ in Fig. 2) as R increases through R_{c1}. It is not energetically allowed into the shallower $2p$ valley ($\alpha \sim \frac{1}{2}\pi$ in Fig. 2), and thus ψ_2 remains identical with $\phi_1(R; \Omega)$ at large R. But as the total energy rises above the $2p\epsilon s$ minimum, ψ_2 is able to spread also into the $2p$ valley at the radius of the avoided crossing. It can thus retain its approximate even (+) symmetry by evolving into an equal superposition of ϕ_1 and ϕ_2, as indicated by the variation of the mixing angle θ shown in Fig. 5. The wave function ψ_1, which originally coincided with $\phi_2(R; \Omega)$, similarly evolves into an odd (−) superposition of ϕ_1 and ϕ_2. The essential result of the hyperspherical approach is thus to identify the limited range of the radial variable $R \sim R_{c\mu}$ and of the energy $-0.1 \leqslant \epsilon_1 \leqslant 0.0$ Ry at which mixing of the $2s$ and $2p$ levels occurs in the eigenchannels.

Further illustration of the preceding results emerges by comparing them with the recent *ab initio* calculation of quantum defect parameters for Ca, Sr, and Ba in Ref. 24. This reference tabulates μ_1, μ_2, θ, and their derivatives with respect to energy at only one energy, the ionization threshold. Extrapolation of these data to lower energy would fail to reproduce the dramatic change of the parameters through the range of avoided crossing, which is shown in Fig. 5. For Be this

variation should emerge by extending the calcula-
tion of Ref. 24 to lower energies point by point.
A comparison would then be possible between the
hyperspherical method and the approach utilized
in Ref. 24 to represent effects of electron cor-
relation in the valence shell.

D. "Elimination" of the closed $2p\epsilon s$ channel

The short-range parameters of Fig. 5 specify
the asymptotic form of the ψ_α when combined with
the known behavior of the Coulomb functions in Eq.
(22). Each of the functions (f_2, g_2) diverges as
$R \to \infty$ for any energy below the $2p$ threshold. The
first step required to satisfy any physically
allowed boundary condition is to superpose the ψ_α
so as to ensure the vanishing of these diverging
components. Imposition of this requirement, and
of the further stipulation that the channel 1 com-
ponents remain energy normalized, effectively
eliminates the closed channel 2. The wave func-
tion has then the form

$$\psi = a_1 \psi_1 + a_2 \psi_2 ,$$

with the asymptotic expansion

$$\psi \xrightarrow[R \to \infty]{} \phi_1 f_1(R) \cos\delta - \phi_1 g_1(R) \sin\delta + O(\exp(-R/\nu_2)) ,$$
(29)

where the "eigenphase shift" of the lower channel
is

$$\tan\delta = \frac{\sin\pi\mu_1 \sin\pi(\nu_2 + \mu_2) + \tan^2\theta \sin\pi\mu_2 \sin\pi(\nu_2 + \mu_1)}{\cos\pi\mu_1 \sin\pi(\nu_2 + \mu_2) + \tan^2\theta \cos\pi\mu_2 \sin\pi(\nu_2 + \mu_1)} ,$$
(30)

and the coefficients of superposition are

$$a_1 = \sin(\pi\mu_1 - \delta)/\sin\theta \sin\pi(\mu_1 - \mu_2) ,$$

$$a_2 = -\sin(\pi\mu_2 - \delta)/\cos\theta \sin\pi(\mu_1 - \mu_2) .$$
(31)

By this elimination of the closed channel, the
problem is reduced to the simpler single-channel
form, with effects of the closed channel embodied
in the energy dependences of δ, a_1, and a_2. The
Be $^1P^0$ eigenphase shift δ is shown in Fig. 6.
Bound states below the Be$^+$ $2s$ level occur at en-
ergies where

$$\delta/\pi + \nu_1 = \text{integer} .$$
(32)

The lowest three bound levels are given in Table
III. Comparison with Table II shows the agreement
with the experimental levels to be greatly im-
proved over the adiabatic values, although the er-
ror in μ (ranging from 0.06 to 0.11) remains large
compared to the state-of-the-art calculations. The
comparison also verifies the interpretation in
item (b) of Sec. III C of the large jump of the $2s3p$
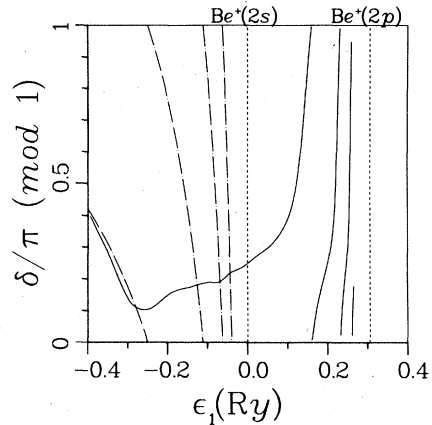quantum defect from the $2s2p$ value as the sig-

FIG. 6. Be eigenphase shift of the lower $(2s\epsilon p)$ chan-
nel obtained by "eliminating" the upper $(2p\epsilon s)$ channel
through Eqs. (29)–(31). Intersections with the dashed
curves $n-\nu_1$ locate the $2snp$ bound levels.

nature of strong channel mixing.

The rapid rises of δ by π above the Be$^+$ $(2s)$ level
are associated with the autoionizing $2pns$ levels,
which dominate the scattering and photoabsorption
cross sections in this energy range. When com-
bined with the pure Coulomb scattering amplitude,
δ determines the $^1P^0$ contribution to the e-Be$^+$
elastic scattering cross section in the energy
range between the $2s$ ground state and the $2p$
level of Be$^+$. The Coulomb divergence dominates
the small angle scattering at all energies, but at
larger angles the rapid energy dependence of δ
causes the cross section to be dominated by strong
autoionizing resonances.[49]

E. Photoionization of Be: The autoionization spectrum

Absorption of photons linearly polarized along
the z axis depends on two dipole-matrix elements,

$$D_\alpha = \langle\psi_\alpha | R \cos\alpha \cos\theta_1 + R \sin\alpha \cos\theta_2 | \psi_0\rangle , \quad (33)$$

where ψ_0 is the Be $2s^2$ ground-state wave function
and ψ_α $(\alpha = 1$ or $2)$ is the energy-normalized $^1P^0$
final-state wave function with the asymptotic form
given by Eq. (23). The ground-state wave function
ψ_0 decays exponentially at large R, and hence the
matrix elements D_α depend on the small-R portion
of ψ_α only. The D_α, as shown in Fig. 7, are thus
smooth functions of energy across ionization

TABLE III. $2snp$ $^1P^0$ discrete levels of Be, including
channel coupling (this work).

Level	Quantum defect
$2s2p$	0.110
$2s3p$	0.181
$2s4p$	0.202
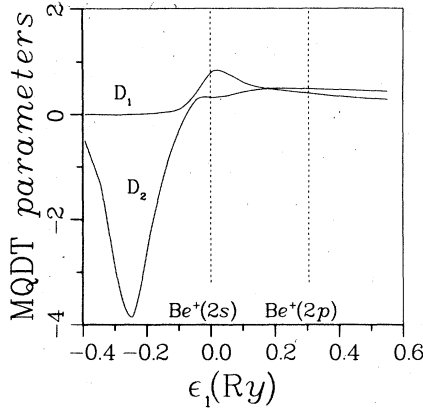
FIG. 7. Calculated dipole-matrix elements D_α for photoionization of Be, as functions of energy ϵ_1.

thresholds, just as μ_1, μ_2, and θ are in Fig. 5.

Below the $2s$ threshold D_2 attains large negative values, peaking near the $2s2p$ level of Be at $\epsilon_1 \sim -0.25$ Ry. This peak is followed by a drop in magnitude at higher energies and a sign change at $\epsilon_1 \sim -0.08$. This energy dependence occurs also for a single electron and in an independent electron model, and gives rise to "Cooper minima" in the photoabsorption spectrum of almost every atom, here occurring at $\epsilon_1 \sim -0.08$. This qualitative behavior is interpreted in Ref. 50 in terms of the energy-dependent nodal structure of the escaping photoelectron's wave function, and is by now well understood and documented. In the energy range below this minimum, it is D_2 that is large and not D_1 because $\alpha = 2$ corresponds to the $2s\epsilon p$ channel (just as μ_2 corresponded to channel 1 in Fig. 5). The higher mock-centrifugal barrier of the $2p\epsilon s$ potential curve allows little overlap of ψ_1 with ψ_0, which keeps D_1 small until the channel mixing becomes significant at $\epsilon_1 \gtrsim -0.10$.

The two dipole amplitudes D_1 and D_2 combine with the parameters of Fig. 5 to determine the photoabsorption spectrum over the energy range shown in Fig. 7. In terms of the a_1, a_2, and δ in Eqs. (30) and (31) the cross section is given by different expressions depending on how many channels (0, 1, or 2) are open in the final state:

(a) Both channels are closed ($\epsilon_1 \le 0$). The photoabsorption in this range occurs only at the bound-state energies, where the effective quantum number ν_1 satisfies

$$\nu_1 + \delta/\pi = n .\qquad(34)$$

Then the photoabsorption cross section of each level is given in a.u. by

$$\sigma_n = (4\pi^2\omega/137)(a_1 D_1 + a_2 D_2)^2/N_n^2 ,\qquad(35)$$

where

$$N_n^2 = \nu_{1n}^3 + \pi^{-1}d\delta/d\epsilon_1 .\qquad(36)$$

ω is the proton energy in a.u., a_1 and a_2 are given by Eq. (31).

(b) One channel $(2s\epsilon p)$ is open $(0 \le \epsilon_1 \le 0.306$ Ry). Here, the total cross section is a continuous function of ω and is given by (35) with $N_n^2 = 1$:

$$\sigma = (4\pi^2\omega/137)(a_1 D_1 + a_2 D_2)^2 .\qquad(37)$$

(c) Both channels are open ($\epsilon_1 \ge 0.306$ Ry). The total cross section is now

$$\sigma = (4\pi^2\omega/137)(D_1^2 + D_2^2) .\qquad(38)$$

The partial cross sections for leaving the Be^+ ion in the alternative $2s$ or $2p$ levels are given by

$$\sigma_{2s} = r\sigma/(1+r), \quad \sigma_{2p} = \sigma/(1+r) ,\qquad(39)$$

where the branching ratio is

$$r = \frac{D_1^2\cos^2\theta + D_2^2\sin^2\theta + D_1 D_2\sin2\theta\,\cos\pi(\mu_1 - \mu_2)}{D_1^2\sin^2\theta + D_2^2\cos^2\theta - D_1 D_2\sin2\theta\,\cos\pi(\mu_1 - \mu_2)} .$$

$$(40)$$

The photoionization cross section in Regions (b) and (c), calculated from Eqs. (37) and (38), is plotted in Fig. 8(a) and shows generally good agreement with the previous close-coupling result of Dubau and Wells[23] [Fig. 8(b)]. This spectrum has been measured experimentally by Mehlman-Balloffet and Esteva,[8] but it is not absolute nor is it very clean, so it is not shown here. Still, the experimental spectrum agrees with the general shape of both results in Fig. 8. The most striking feature of Fig. 8 is the series of very strong $2pns$ autoionizing resonances, whose widths are comparable to their separations. The $2p3s$ resonance has a full width at half maximum of $\Gamma \sim 1.3$ eV, which is enormous compared to typical resonances in small atoms.

The plotted spectrum includes only the lowest three $2pns$ resonances, though they belong to an infinite series converging to the Be^+ $(2p)$ level. Just below this threshold their average absorption is given by a smooth backward extrapolation of the cross section above threshold, as shown by Gailitis.[51] It is clear from the overall appearance of the total cross section in Fig. 8 that the doubly excited $2pns$ levels absorb photons with an intensity comparable to the $2s\epsilon p$ continuum. Evaluation of Eq. (40) for the branching ratio at the $2p$ threshold demonstrates this quantitatively, giving for the partial photoionization cross sections into singly excited and doubly excited channels: $\sigma_{2s} = 1.02$ Mb and $\sigma_{2p} = 0.57$ Mb, respectively.

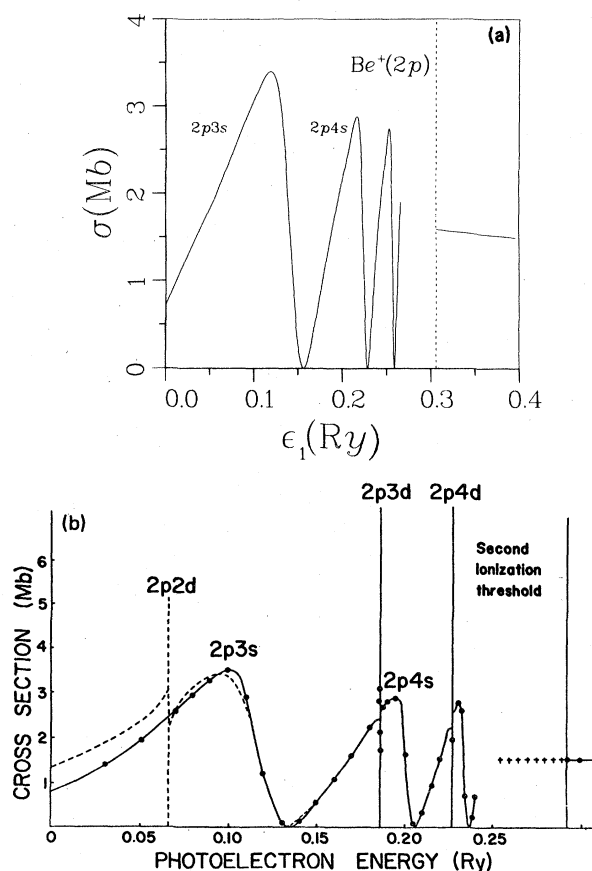One feature of Fig. 8(b) absent from Fig. 8(a) is

FIG. 8. Total cross section for Be photoionization versus energy of the photoelectrons ϵ_1. (a) Present hyperspherical calculation, (b) Dubau-Wells close-coupling calculation (Ref. 23).

the series of narrow $2pnd$ resonances, which belong to the $2p\epsilon d$ potential curve of Fig. 1(c). They were not included in my calculation for simplicity as they are so narrow and perturb the spectrum so weakly. It should be straightforward to obtain these narrow lines by extending the present treatment to include all three channels. Note also that a "spurious" resonance $2p2d$ occurs in the dashed curve of Fig. 8(b), which was obtained in Ref. 23 by extrapolating the short-range MQDT parameters backward from the $2p$ threshold. Such unphysical resonances can be avoided by incorporating in the extrapolation the energy dependence of the eigenquantum defects far below threshold, described in item (a) of Sec. III C.

F. Connection with the discrete spectrum: A new interpretation of the oscillator strength distribution

The similarity of Eqs. (35) and (37) shows that photoabsorption just below the $2s$ threshold is closely related to photoionization just above this

threshold, differing only in N_n^2 which converts from an energy-normalized wave function to a wave function normalized to unity. This analytical relationship between the discrete and continuum is exploited in graphical presentations of the discrete spectrum (Fig. 1 of Ref. 50). The cross section (or the equivalent oscillator strength) is shown below threshold as a histogram, each block of which represents a discrete level. Since the height of each block is set equal to $\sigma_n N_n^2$, the histogram joins smoothly at threshold to the photoionization cross section above threshold. One may instead simply plot the continuous function $\sigma(\epsilon_1)$ given by Eq. (37) below the $2s$ threshold as well as above. This gives a continuous "energy-normalized cross section" below threshold which joins to the continuum smoothly, as shown for Be in Fig. 9. It must be remembered, of course, that Be photoabsorption selects only a discrete set of energies from this graph (the lowest three levels were given in Table III.) At those energies the actual cross section is obtained by dividing $\sigma(\epsilon_1)$ by N_n^2.

In Fig. 9, σ peaks strongly near the $2s2p$ energy ($\epsilon_1 = -0.29$ Ry), which makes $2s2p$ look like a natural continuation of the $2pns$ autoionizing series above Be$^+$ ($2s$). Thus for Be the Cooper minimum[50] at $\epsilon_1 = -0.08$ Ry coincides with the Beutler-Fano minimum[52] due to sp-ps coupling which lies between the $2s2p$ and $2p3s$ maxima. (It must be remembered, however, that the Cooper minimum is present even in the absence of channel coupling, so the channel interaction primarily shifts this minimum.) This casts the $2s2p$ state as a "member" of the $2pns$ Rydberg series, a concept totally foreign to traditional spectroscopy. Further evidence for this conclusion is shown in Table IV, which compares the experimental quantum defects of the $2pns$ levels with the $2s2p$ quantum defect, but referred to the $2p$ threshold instead of the $2s$ threshold as in Table II. Note that the $2s2p$ quantum defect (referred to $2p$) agrees much better with those of $2pns$ states than the $2s2p$ quantum defect (referred to $2s$) agrees with the $2snp$ quantum defects in Table II.

Though this assignment differs from that of traditional spectroscopy it arises naturally in the hyperspherical picture, as an analog of the crossing of "+" and "$-$" potential curves for He and H$^-$. Thus in He the lowest-lying $^1P^0$ state ($2s2p$) belongs to the "+" Rydberg series, while for Rydberg levels nearer threshold the "$-$" channel is more attractive and its levels are lower. For Be the two relevant curves do not cross, though a remnant of the crossing remains apparent in Fig. 2, through inspection of the number of nodes in $g_\mu^{1/2}(R; \alpha)$ as R increases. The crossing is also
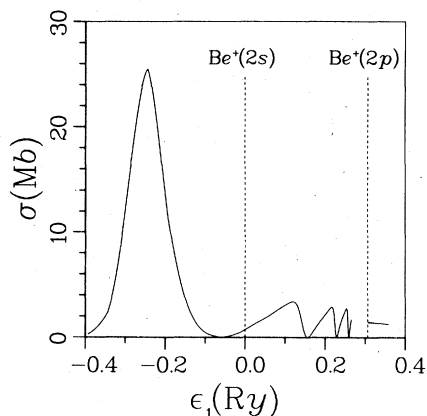
FIG. 9. Be photoabsorption cross section including the discrete absorption calculated using energy-normalized wave functions. See text for details.

reflected in the diabatic crossover of intensity in Be, where $2s2p$ and the $2pns$ states absorb photons strongly like He "+" states while the $2snp$ discrete states $(n>2)$ and $2s\epsilon p$ continuum absorb weakly like He "−" states. Table V compares several calculated discrete oscillator strengths with previous results, showing a verification of the qualitative features, though the quantitative agreement is worse here than for the autoionizing spectrum of Fig. 8.

Finally, it should be pointed out that the continuous cross section $\sigma(\epsilon_1)$, shown below the $2s$ threshold in Fig. 9, may be experimentally observable even *away* from the discrete levels. A new experimental technique developed by Cole et al.[53] lowers the ionization threshold by applying a static electric field to the atom, which allows the discrete oscillator strength to be smeared out and observed as a continuum. Section IV B will point out similar intensity "crossovers" observed in photoabsorption spectra of other atoms.

IV. RELATED SYSTEMATICS OF OTHER TWO-ELECTRON SYSTEMS

The quantitative mapping of electron correlations in the Be sp valence shell has clarified the connection between the broad autoionizing states and the irregularly spaced discrete states. In view

TABLE IV. Experimental $2pns$ $^1P^0$ Be quantum defects (Ref. 8).

Level	Quantum defect
$2s2p$	0.71
$2p3s$	0.7
$2p4s$	0.78
$2p5s$	0.74

TABLE V. Discrete $2s^2$-$2snp$ $^1P^0$ oscillator strengths of Be.

Level	Hyperspherical, f_n	(Ref. 12) f_n
$2s2p$	0.68	1.71
$2s3p$	0.017	0.0030
$2s4p$	0.0002	0.0007

of this experience gained in Sec. III, I will now attempt to interpret related properties of the alkaline-earth atoms and alkali negative ions.

A. MQDT parameters of the large alkaline earths

Though each of the alkaline-earth atoms has the same ns^2 ground-state designation, their core structures differ considerably. This is clear from Table VI, which gives the lowest s, p, and d energy levels of their singly charged positive ions. The first excited state of the lightest two ions Be$^+$ and Mg$^+$ is the np state, while it is $(n-1)d$ for the remaining "heavy" alkaline-earth ions Ca$^+$, Sr$^+$, Ba$^+$, and Ra$^+$. Accordingly, the spectra of Be and Mg are similar, but they differ qualitatively from spectra of Ca, Sr, Ba, and Ra which are similar among themselves.

The lowest four $^1P^0$ potential curves for Ca are shown in Fig. 10.[54] The lowest doubly excited channel is now $3d\epsilon p$ whose potential minimum lies far below the Ca$^+$($4s$) threshold, in fact, midway between the $4s4p$ and $4s5p$ bound levels. Accordingly, the $4snp$ levels $(n \geq 5)$ all mix strongly with the $3d\epsilon p$ channel, as is verified by the Lu-Fano plot of $^1P^0$ Ca levels[13(b)] in the inset of Fig. 10. This plot shows a rise by nearly unity of the quantum defect [which coincides with δ/π defined by Eq. (30)] between the $4s5p$ level and the ionization threshold; this rise is centered on the fourth bound level, which is thus labeled $3d4p$ in accordance with Ref. 13(b) but in contrast to the standard Ref. 10. However, this lowest doubly excited level is in fact distributed over the entire $4snp$ Rydberg series, and represents only a small portion of any particular bound state. The occurrence of doubly excited levels in the discrete spectrum is common to Ca and to the heavier alkaline earths while all doubly excited levels in Be and

TABLE VI. Experimental ion energy levels (in Ry).

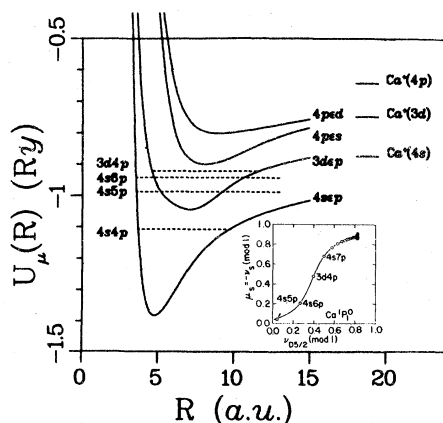| Ion	n	ns	np	$(n-1)d$
Be$^+$	2	−1.338	−1.047	−0.444
Mg$^+$	3	−1.105	−0.779	−0.454
Ca$^+$	4	−0.873	−0.642	−0.748
Sr$^+$	5	−0.811	−0.590	−0.677
Ba$^+$	6	−0.735	−0.540	−0.686

FIG. 10. Calcium $^1P^0$ adiabatic potential curves calculated using the new semiempirical method of Watanabe (Ref. 54). The lowest four experimental bound levels are shown as dashed lines contained within the appropriate potential curve. The inset is a Lu-Fano plot of $-\nu_1 = -\nu_s$ versus $\nu_2 = \nu_D$ for these bound levels from Ref. 13(b).

Mg are above threshold.

Figure 10 indicates that the $4p\epsilon s$ potential curve is repelled strongly by $3d\epsilon p$ through a channel mixing, while $4p\epsilon d$ varies more smoothly with R reflecting a weaker channel mixing. The $4p\epsilon s$ potential minimum lies close to the $4s$ threshold; its mixing with $4s\epsilon p$ and $3d\epsilon p$ is then expected to become important at this energy as in Be and Mg. A sensible *ab initio* calculation of the Ca spectrum must include the $4p\epsilon s$ channel in order to obtain realistic results above the $4s$ threshold.

The energy dependence of μ_1, μ_2, and θ should accordingly be similar for the lowest two channels in all of the alkaline-earth atoms, though the onset of channel mixing occurs at lower energies in the heavier atoms. A calculation analogous to that of Be would be required to predict the values of these parameters, and their dependence on the specific electron correlations in each atom, but Ref. 13 has found that the mixing angles θ and the differences of eigenquantum defects $\Delta = \mu_1 - \mu_2$ are nearly identical for Ca, Sr, Ba, and Ra. This regularity emerges from Table VII, which also includes the Be parameters taken from Fig. 5 at

TABLE VII. Short-range scattering parameters of the $^1P^0$ alkaline earths (Ref. 13).

Atom	θ/π	$\Delta = \mu_1 - \mu_2$	$\bar{\mu} = \frac{1}{2}(\mu_1 + \mu_2)$	$\|S_{12}\|^2$
Be	0.29	0.40	0.33	0.85
Ca	0.33	−0.42	0.78	0.72
Sr	0.30	−0.44	0.71	0.87
Ba	0.30	−0.40	0.63	0.82
Ra	0.30	−0.35	0.57	0.72

the $2p$ threshold. Moreover, the regularity extends to the Be parameters with unexpected quantitative accuracy, except for the sign difference of Δ for Be.

In the absence of calculations for Ca, Sr, Ba, and Ra as complete as for Be, the following interpretation of the near equality of θ and D for these atoms reported in Ref. 13 is necessarily tentative. The localized, strongly avoided crossing of the calcium potential curves $4s\epsilon p$ and $3d\epsilon p$ in Fig. 10 suggests that the mixing of these channels at $R \gtrsim R_{c\mu}$ has the effect of preserving diabatically the character of the wave functions ψ_1 and ψ_2 which was established in the adiabatic short-range region $(R < R_{c\mu})$ in Be. Note that in Be the "+" or "−" symmetry character is also preserved diabatically through the avoided crossing but without any need for channel mixing. The coincidence of the He$^+$ levels $2s$ and $2p$ allows each adiabatic state ϕ_μ to retain the ± symmetry at all R except in the immediate proximity of the narrowly avoided crossing; a diabatic transition through this crossing implies merely a sudden switch from one ϕ_μ to the other, in contrast to the mixing that occurs in the alkaline earths.

B. Photoabsorption spectrum of Mg and Ne

The structure of Mg is sufficiently similar to Be to permit a discussion of outstanding features of its spectrum in the absence of a coupled-channels calculation. Yet such a discussion is nontrivial, as Mg differs from Be in important ways. The main difference is the presence in Mg of a larger closed shell $2p^6$ core, which makes the Mg$^+$ ion "softer" than Be$^+$ as evidenced by its lower binding energies in Table VI. Thus the $3s$ level of Mg$^+$ is less strongly bound than the $2s$ of Be$^+$. On the other hand the Mg$^+$ $3p$-$3s$ separation, is 0.035 Ry larger (12%) than the Be$^+$ $2p$-$2s$ separation, reflecting that the field within the Mg^{++} core is far less hydrogenic than for Be^{++}.

The $3s\epsilon p$ and $3p\epsilon s$ potential curves of $^1P^0$ Mg are shown in Fig. 11. The most obvious change from Be results of Fig. 1(c) is an expansion of the radial range, as the $3p\epsilon s$ minimum occurs at $R \sim 6$ for Mg while the corresponding $2p\epsilon s$ Be minimum occurs at $R \sim 5$. More important is that the $3p\epsilon s$ minimum lies very close to the Mg$^+$ $3s$ level, whereas the $2p\epsilon s$ minimum in Be is about 0.14 Ry *lower* than the $2s$ level of Be$^+$. Accordingly the strong coupling transition of the mixing angle from $\frac{1}{2}\pi$ to $\sim \frac{1}{4}\pi$ should occur at a much higher energy in Mg, near Mg$^+$ ($3s$).

The photoabsorption spectrum of Mg has been calculated by Altick and Bates, and is shown in Figs. 3 and 4 of Ref. 25. Some experimental mea-
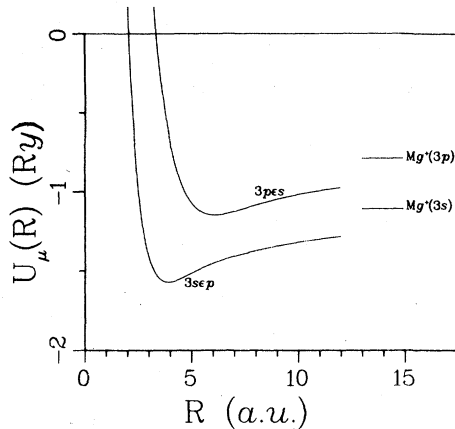
FIG. 11. Magnesium $^1P^0$ adiabatic potential curves.

surements are known[8] but as for Be they are only relative and are not very clean. The shape of the Mg spectrum of Ref. 25 is quite similar to the Be spectrum shown in Fig. 9. For example, Mg also has a maximum absorption near the lowest ($3s3p$) discrete level, and shows a series of very broad $3pns$ autoionizing resonances converging to the $3p$ threshold. There are, however, two related major differences from the Be spectrum:

(a) The Cooper minimum occurs at a higher energy in Mg than in Be. While the Be minimum occurred among the $2snp$ discrete levels at $\epsilon_1 \sim -0.07$ Ry, it occurs in the continuum at $\epsilon_1 \sim 0.12$ Ry above the $3s$ threshold for Mg.

(b) The discrete states of Mg have a larger fraction of the total oscillator strength than the discrete states of Be. Thus the oscillator strength above threshold is depressed in Mg, as evidenced by the lower peak absorption of the Mg autoionizing resonances, which is only 1 Mb compared to 3.5 Mb in Be.

Here, (a) is primarily a one-electron effect, related to the presence (or absence) of the $2p^6$ core for Mg (or Be). Thus the Cooper minimum for Na also occurs above threshold in contrast to Li where it lies below. Item (b) follows in part from (a). That is, since the oscillator strength goes throgh zero *below* threshold for Be but not for Mg, it is natural to expect the discrete spectrum of Mg to have a generally stronger photoabsorption than Be while its continuum should be weaker. What is new here is that the accumulation of oscillator strength in the discrete spectrum of Mg is also reflected in a depression of photoabsorption by the doubly excited $3p\epsilon s$ channel. That is, the ratio σ_{3p}/σ_{3s} above the $3p$ threshold is expected to be smaller for Mg than the ratio found earlier of $\sigma_{2p}/\sigma_{2s} = 0.56$ for Be, though this ratio in Mg has apparently never been measured or calculated. The larger separation of the two Mg potential

curves has thus nearly eliminated the diabatic crossover of the oscillator strength which was seen so strongly in Be. This conclusion is also supported by noting that the $3s3p$ quantum defect agrees with those of the $3snp$ levels much better than for the $3pns$ autoionizing levels, also in contrast to Be.

The mixing of $3p\epsilon s$ and $3s\epsilon p$ channels has also been observed in neon photoabsorption, where, however, the intensity crossover resembles that of Be more than that of Mg. This spectrum was observed long ago by Codling *et al.*[55] using synchrotron light to measure neon photoabsorption in the photon wavelength range 200 to 280 Å, which reaches the doubly excited $3snp$ and $3pns$ configurations. The experimental findings[55] can be summarized as follows. The $3s3p$ state absorbs light strongly, but the $3s4p$ level is so weak that it is missing from the spectrum entirely. A weak series of levels then reappears, beginning with $3s5p$, but with a completely different autoionization line shape. Finally, the $3pns$ autoionizing states with $n \geq 4$ absorb strongly above the $3s$ threshold, and interestingly enough their line profile is similar to that of $3s3p$. This suggests that, as in Be, the $3s3p$ and $3pns$ have "+"-type characteristics, whereas the $3snp$, $n \geq 4$, are "$-$"-type states. A remark to this effect was included in Ref. 55.

Neon is much more complicated than the alkaline earths in this energy range, since the outermost two electrons move in the field of a softer, *open-shell* core, $(2p^4)^3P^e$. A further complication is that the outermost two sp electrons are classified as $^3P^0$, which is necessary if the combined state of *all* electrons is $^1P^0$. Since "+" and "$-$" do not cross for $^3P^0$ helium, it is not clear why they should do so for neon. It remains for future calculations to investigate the nature of this crossover of intensity and profile characteristics for neon.

C. Photodetachment of alkali negative ions

Photodetachment experiments[15] performed near the threshold for core excitation to its first excited state (np) show narrow Feshbach resonances with autodetaching strengths that are much larger than for H[-] even though small because of proximity to threshold. These resonances have been identified[16] as having primarily an $np\epsilon s$ $^1P^0$ classification. The $^1P^0$ potential curves of K[-] in the relevant energy range are shown in Fig. 1(d). The +/$-$ crossing is absent here as in Be since the $4s$ and $4p$ levels of potassium are not degenerate. The resemblance of Figs. 1(c) and 1(d) suggests that for energies near the $4p$ level of K and above the

$4p\epsilon s$ potential curve minimum, the two channels $4s\epsilon p$ and $4p\epsilon s$ will be strongly coupled nonadiabatically with nearly equal mixing, $\theta_{eq} = \frac{1}{4}\pi$. At large radial distances the Coulomb attraction is absent, so the wave functions (f_i, g_i) of Eq. (23) are to be interpreted here as spherical Bessel functions [renormalized to be energy independent at $r = 0$ (Ref. 17, 46)] rather than Coulomb functions. With this obvious modification, the solution of the coupled Eqs. (17) could proceed just as described for Be, giving the five $^1P^0$ short-range MQDT parameters μ_1, μ_2, θ, D_1, and D_2 which then determine the cross section.

To interpret the Cs$^-$ spectrum for the first time, Lee[17] fitted these parameters (assumed constant) to experimental results and obtained good agreement. (In addition $^3P^0$ parameters also had to be fitted since the spin-orbit interaction couples $^1P^0$ to $^3P^0$ strongly closely to threshold. Here, I will focus on the $^1P^0$ parameters only for comparison with the parameters in Table VII.) Lee's Cs$^-$ values are compared with the *ab initio* K$^-$ values at the $4p$ threshold in Table VIII, which shows that nearly equal mixing is also obtained for the alkali negative ions just as for the alkaline-earth atoms of Table VII. This agreement verifies that the potential ridge ($\alpha = \frac{1}{4}\pi$, $\theta_{12} = \pi$) splits the wave function almost equally into the two potential valleys here as in Be.

The *ab initio* values of Norcross and Taylor[26] show a strong energy dependence which is not relevant here, as discussed in Ref. 27. This reference calculated the effect of the alkali polarizability on negative ion photodetachment by using the exact regular and irregular Mathieu function solutions (f_i, g_i) of the polarization Schrödinger equation, instead of the spherical Bessel functions used by Refs. 17 and 26. In this "polarization representation" the parameters of K$^-$ are constant over the 50-meV range of interest near K($4p$) with values $\mu_1 = 0.48$, $\mu_2 = -0.25$, and $\theta = 0.08\pi$. The large change of this mixing angle from the "zero-field representation" of Table VIII implies that the channel couplings depend sensitively on the long-range field effects built into the base pair (f_i, g_i).

V. DISCUSSION

The preceding sections I–IV have developed a generalization of the hyperspherical method appropriate for the analysis of correlations between two electrons outside a many-electron closed-shell ionic core. This treatment has focussed on low-energy double excitations, without attempting to encompass the Wannier phenomena[32-35] associated with the higher energy range in which both electrons have sufficient (or nearly sufficient) energy to escape the atom. A main conclusion of Sec. III is that strong intrashell excitations (such as the $2s$-$2p$ excitation of Be$^+$) can be regarded as a localized departure from an otherwise adiabatic evolution in R along the hyperspherical potential curves $U_\mu(R)$. A ripe problem is the extension of this approach to treat the strong mixing of channels in other groups of atoms, such as the aluminum[56] $3s^2\epsilon d$ and $3s3p\epsilon p$ $^2D^e$ channels. This aluminum example involves all *three* outer electrons equally, and thus requires a substantial new developement. A preliminary hyperspherical study of such three-electron systems has recently been applied to Li,[57] but it is not yet suited for quantitative calculations.

The line of research described here is designed primarily to interpret the gross systematics of electron correlations over a broad range of energies. Over narrow ranges of energy instead, weaker forces (mainly spin orbit) can drastically perturb the spectrum.[15] These weaker forces usually become noticeable when the spectrum is examined with fine resolution close to ionization thresholds. This class of effects is to be handled separately from those considered here, using as input calculations like the present one for Be. These weak interactions should cause avoided crossings (for example, between $^1P^0$ and $^3P^0$ potential curves in K$^-$) at much larger R than the crossings having an electrostatic origin. However, it should not be necessary to develop a full relativistic generalization of the present method which treats all such effects simultaneously. Indeed, it appears advantageous to handle separately effects of such different dynamical origin and influence.

The different alkaline-earth atoms, while similar in their overall spectra illustrate three distinct regimes in their manifestations of electron correlations in the discrete spectrum. At one extreme is Mg, which has widely separated $ns\epsilon p$ and $np\epsilon s$ $^1P^0$ potential curves; thus the usual discrete spectrum of $nsmp$ levels is little affected by mixings with the doubly excited $np\epsilon s$ channel containing the higher-lying $npms$ autoionizing levels. At the opposite extreme are the heavy alkaline earths Ca, Sr, Ba, and Ra, which have a much lower-lying doubly excited potential curve [although of a different configuration than Mg and Be, namely $(n-1)d\epsilon p$]. Thus throughout the discrete spectrum of these atoms, the mixing with

TABLE VIII. $^1P^0$ scattering parameters of the alkali negative ions (Refs. 17 and 27).

Ion	θ/π	$\Delta = \mu_1 - \mu_2$	$\bar{\mu} = \frac{1}{2}(\mu_1 + \mu_2)$
K$^-$	0.26	0.03	0.49
Cs$^-$	0.22	-0.02	0.49

this doubly excited channel is apparent, in parti-
cular because the discrete spectrum even con-
tains doubly excited "perturber" levels. Finally,
Be is intermediate between these two groups,
though closer to Mg. That is the channel mixing
sets in at a lower energy in Be than in Mg, near
the second discrete level $2s3p$ causing a "jump"
in its quantum defect, but the $2pns$ doubly excited
levels remain well above the $2s$ threshold as in
Mg.

As the energy increases significantly above the
asymptotic threshold of each hyperspherical po-
tential curve, the nonseparability in R, α, and θ_{12}
becomes more apparent, especially at small R
where the mock-centrifugal barrier is far too
repulsive.[58] With increasing energy, therefore,
this nonseparability is included in the hyperspher-
ical formulation as a weak nonadiabatic coupling
to a large number of higher-lying potential curves
which may nevertheless have a large cumulative
effect. To avoid this inefficient coupling of a large
number of potential curves at higher energies,
Ref. 7 outlined an alternative approach. This
method solves the small-R Schrödinger equation
variationally within $R < R$, by an R-matrix tech-
nique.[44] This portion of the calculation then pro-
vides an input boundary condition for a few-cou-
pled-channels integration as in Sec. III but starting
from $R = R_i$ instead of $R = 0$. An exploration of
this approach for He has been carried out, but
will be reported elsewhere. The nonadiabatic
couplings do have an important effect at small R
as the energy increases above threshold, and a
small-scale R-matrix solution handles them ef-
ficiently. However, up to ~3 eV above threshold
the couplings do not have a strong qualitative ef-
fect on the dynamics, and so this R-matrix so-
lution in the "core" region $R < R_i$ $(R_i \sim 3$ a.u.) was
not utilized for the Be calculation of Sec. III.

Finally, extensive measurements have been
made, largely by Gallagher,[18] of the optical ex-
citation functions of the alkali-metal resonance
lines by electron impact. The wealth of these ex-
perimental data is concentrated mainly at higher
energies than treated in this article. Thus an in-
terpretation of these experiments should be feasi-
ble once the R-matrix treatment of the core region
is more fully implemented and combined with the
coupled-channels approach used here.

Note added in proof. Two extremely relevant
articles were inadvertently omitted in the above
discussion. Firstly, the work of J. Geiger[59] dem-
onstrated semiempirically how an *energy-depen-
dent* mixing angle is needed to reproduce the ob-
served oscillator strength distribution of calcium.
Secondly, the beryllium oscillator strengths of
Table V should be compared with the accurate
values obtained by Lin and Johnson[60] using the
relativistic random phase approximation. Their
results, which should have state-of-the-art pre-
cision, are $f_n = 1.38$, 0.025, 0.0013 for the $2s2p$,
$2s3p$, and $2s4p$ levels of Be, respectively. It is
suspected that numerical inaccuracies in the R
integration far below threshold caused the large
(50%) error in the $2s2p$ hyperspherical oscillator
strength given in Table V, since the results for
the higher levels and the continuum agree rea-
sonably well with previous calculations. However,
since this discrepancy does not affect the main
conclusions drawn here, the issue has not been
pursued.

ACKNOWLEDGMENTS

*Present address: Department of Chemistry, Stanford
University, Stanford, California, 94305.
[1]R. P. Madden and K. Codling, Phys. Rev. Lett. 10, 516
(1963); Astrophys. J. 141, 364 (1965).
[2]P. G. Burke and P. D. McVicar, Proc. Phys. Soc.
London 86, 989 (1965).
[3]P. L. Altick and E. N. Moore, Phys. Rev. Lett. 15, 100
(1965); Phys. Rev. 147, 59 (1966); L. Lipsky and A.
Russek, *ibid.* 142, 59 (1966); T. F. O'Malley and S.
Geltman, *ibid.* 137, A1344 (1965).

[4]J. H. Macek, J. Phys. B 1, 831 (1968).
[5]U. Fano, in *Atomic Physics I,* edited by B. Bederson,
V. W. Cohen, and F. M. Pichanick (Plenum, New York,
1969), p. 209; see also U. Fano, Physics Today 29,
No. 9, 32 (1976).
[6](a) C. D. Lin, Phys. Rev. A 10, 1986 (1974); (b) *ibid.*
12, 493 (1975); (c) Phys. Rev. Lett. 35, 1150 (1975).
[7]U. Fano, in *Invited Papers and Progress Reports of
the Tenth ICPEAC* edited by G. Watel (North-Holland,
Amsterdam, 1978), p. 271.

[8]G. Mehlman-Balloffet and J. M. Esteva, Astrophys. J. 157, 945 (1969).

[9]C. M. Brown and M. L. Ginter, J. Opt. Soc. Am. 70, 87 (1980); ibid. 68, 817 (1978).

[10]C. E. Moore, Atomic Energy Levels I–III, Nat'l. Bur. Stnds. (U.S.) Circ. 467 (U.S.G.P.O., Washington, D.C., 1949).

[11]K. T. Lu, J. Opt. Soc. Am. 64, 706 (1974).

[12]P. L. Altick and A. E. Glassgold, Phys. Rev. 133, A632 (1964).

[13](a) J. J. Wynne and J. A. Armstrong, Comments At. Mol. Phys. 8, 155 (1979) and references therein; (b) J. A. Armstrong, J. J. Wynne, and P. Esherick, J. Opt. Soc. Am. 69, 211 (1979); (c) J. A. Armstrong, J. J. Wynne, and F. S. Tomkins, J. Phys. B 13, L133 (1980).

[14]U. Fano, J. Opt. Soc. Am. 65, 979 (1975).

[15](a) J. Slater, F. H. Read, S. E. Novick, and W. C. Lineberger, Phys. Rev. A 17, 201 (1978) and references therein; (b) P. Frey, F. Breyer, and H. Hotop, J. Phys. B 11, L589 (1978).

[16]D. L. Moores and D. W. Norcross, Phys. Rev. A 10, 1646 (1974).

[17]C. M. Lee, Phys. Rev. A 11, 1692 (1975).

[18]S. T. Chen and A. C. Gallagher, Phys. Rev. A 17, 551 (1978), and references therein.

[19]W. Williams and S. Trajmar, J. Phys. B 10, 1955 (1977).

[20]J. O. Phelps, J. E. Solomon, D. F. Korff, C. C. Lin, and E. T. P. Lee, Phys. Rev. A 20, 1418 (1979).

[21]P. Burrows and A. Johnston (private communication).

[22]D. L. Moores, Proc. Phys. Soc. London 91, 830 (1967).

[23]J. Dubau and J. Wells, J. Phys. B 6, 1452 (1973).

[24]K. C. Pandey, S. S. Jha, and J. A. Armstrong, Phys. Rev. Lett. 44, 1583 (1980).

[25]G. N. Bates and P. L. Altick, J. Phys. B 6, 653 (1973); P. L. Altick, Phys. Rev. 169, 21 (1968).

[26]K. Taylor and D. W. Norcross (unpublished).

[27]S. Watanabe and C. H. Greene, Phys. Rev. A 22, 158 (1980).

[28]R. N. Zare, J. Chem. Phys. 45, 1966 (1966); A. W. Weiss, Phys. Rev. A 6, 1261 (1972).

[29]D. R. Flower and M. J. Seaton, Proc. Phys. Soc. London 91, 59 (1967).

[30]A. F. Starace, in Handbuch der Physik, edited by W. Mehlhorn (Springer, Berlin, to be published).

[31]J. W. Cooper, U. Fano, and F. Prats, Phys. Rev. Lett. 10, 518 (1963).

[32]G. Wannier, Phys. Rev. 90, 817 (1953).

[33]A. R. P. Rau, Phys. Rev. A 4, 207 (1971).

[34]R. Peterkop, J. Phys. B 4, 513 (1971).

[35]U. Fano, Phys. Rev. A. (in press).

[36]F. Herman and S. Skillman, Atomic Structure Calculations (Prentice-Hall, Englewood Cliffs, N.J., 1963).

[37]U. Fano and C. D. Lin, Atomic Physics 4, (Plenum, New York, 1975), p. 47.

[38]H. Klar, Phys. Rev. A 15, 1452 (1977); H. Klar and U. Fano, Phys. Rev. Lett. 37, 1134 (1976); H. Klar and M. Klar, Phys. Rev. A 17, 1007 (1978).

[39]M. J. Seaton, Proc. Phys. Soc. London 77, 174 (1961).

[40]M. Gailitis and R. Damburg, Proc. Phys. Soc. London 82, 192 (1963).

[41]A. F. Starace and G. L. Webster, Phys. Rev. A 19, 1629 (1979).

[42]D. Miller and A. F. Starace, J. Phys. B 13, L525 (1980).

[43]P. G. Burke, A. Hibbert, and W. D. Robb, J. Phys. B 4, 153 (1971).

[44]U. Fano and C. M. Lee, Phys. Rev. Lett. 31, 1573 (1973); C. M. Lee, Phys. Rev. A 10, 584 (1974).

[45]K. Smith, The Calculation of Atomic Collision Processes (Wiley, New York, 1971), p. 187.

[46]C. H. Greene, U. Fano, and G. Strinati, Phys. Rev. A 19, 1485 (1979).

[47]C. H. Greene, Phys. Rev. A 22, 149 (1980).

[48]C. H. Greene, Phys. Rev. A 20, 656 (1979).

[49]N. F. Mott and H. S. W. Massey, The Theory of Atomic Collisions, (The Clarendon Press, Oxford, England, 1965), 3rd ed., p. 557.

[50]U. Fano and J. W. Cooper, Rev. Mod. Phys. 40, 441 (1968).

[51]M. Gailitis, Zn. Eksp. Teor. Fiz. 44, 1974 (1963) [Sov. Phys.—JETP 17, 1328 (1963)].

[52]U. Fano, Phys. Rev. 124, 1866 (1961).

[53]B. E. Cole, J. W. Cooper, D. L. Ederer, G. Mehlman, and E. B. Saloman, J. Phys. B 13, L175 (1980).

[54]S. Watanabe, (unpublished). This method uses the experimental levels of Ca$^+$ to specify the radial logarithmic derivative of one electron emerging from the Ca^{++} core. By so doing it eliminates the need for a model potential, though it may lead to inaccuracies in the potential curves at small R.

[55]K. Codling, R. P. Madden, and D. L. Ederer, Phys. Rev. 155, 26 (1967).

[56]C. D. Lin, Astrophys. J. 187, 385 (1974).

[57]C. W. Clark and C. H. Greene, Phys. Rev. 21, 1786 (1980).

[58]This has been stressed by J. H. Macek in private communication and is documented in Ref. 6(b).

[59]J. Geiger, J. Phys. B 12, 2277 (1979).

[60]C. D. Lin and W. R. Johnson, Phys. Rev. A 15, 1046 (1977).